Molecular Physics
Vol. 00, No. 00, Month 200x, 1–20

RESEARCH ARTICLE

Evaluation of second and third dielectric virial coefficients for non-polarizable molecular models

Shu Yang, Andrew J. Schultz, and David A. Kofke*

Department of Chemical and Biological Engineering, University at Buffalo, The State University of New York, Buffalo, NY 14260-4200, USA

(*Received 00 Month 200x; final version received 00 Month 200x*)

The dielectric constant, ϵ, of a dilute vapor can be predicted from an appropriately formulated dielectric virial equation of state (VEOS), but the long-ranged nature of the relevant electrostatic interactions complicates the evaluation of coefficients of this series. We propose a formulation of the second and third dielectric coefficients of a general non-polarizable molecular model that permits their reliable calculation using Mayer sampling Monte Carlo. We demonstrate the approach for three models: dipolar hard spheres; dipolar Lennard-Jones (Stockmayer model); and TIP4P water. The results agree well with available coefficient values in the literature while also having better precision. The coefficients are used to compute ϵ for each model as a function of density, which are compared to data obtained from molecular simulation. The form of the VEOS relating ϵ to density depends on the dielectric constant ϵ' of the embedding medium. Three choices are examined: vacuum ($\epsilon' = 1$), self-consistent ($\epsilon' = \epsilon$), and tin-foil ($\epsilon' = \infty$). The form based on the vacuum boundary is found to be unreliable, losing accuracy at low density and yielding divergent results for ϵ at moderate densities. In contrast, the series formulated using the tin-foil boundary produces reasonably accurate and stable values of ϵ for almost all conditions and models examined here, even when the series is truncated at second order (which itself is shown to be a large improvement over the first-order Clausius-Mossotti-Debye formula).

Keywords: Relative permittivity, virial series, Stockmayer potential, hard spheres, TIP4P water

1. Introduction

In response to an electric field, a dielectric material will redistribute its charges, producing a polarization $\mathbf{P}(\mathbf{r})$ (dipole moment per unit volume) that is proportional to the field $\mathbf{E}$ at each point $\mathbf{r}$:

$$\mathbf{P}(\mathbf{r}) = \chi\epsilon_0\mathbf{E}(\mathbf{r}), \tag{1}$$

where χ is the electric susceptibility and ϵ_0 is the vacuum permittivity. This constitutive equation applies for fields that are not too large, and that are not varying quickly with time. In general, χ is tensorial, but for simple isotropic materials such as considered here, it is a scalar. In practice it becomes useful to introduce the dielectric constant ϵ, or relative permittivity, defined such that $\chi = \epsilon - 1$.

The static dielectric constant has great practical importance in physical chemistry, because it quantifies how a solvent attenuates electrostatic interactions of charged species in solution. It is a material property, and thus it depends on details of the interactions of the constituent molecules. The dielectric constant is also a function of temperature and density. For dielectric systems such as water, matching experimental values of the dielectric constant is considered a key test of the quality of a molecular model. Such a comparison may be facilitated using molecular simulation [1], which evaluates the dielectric constant by averaging the squared fluctuating dipole moments in the system [2]. Simulation methods are generally reliable, but they may be expensive because calculations of the dielectric constant are slow to converge, as for any fluctuation-based quantity. On the other hand, an

*Corresponding author. Email: kofke@buffalo.edu

ISSN: 0040-5167 print/ISSN 1754-2278 online

DOI: 10.1080/0040516YYxxxxxxxx
http://www.informaworld.com

alternative formulation of the relevant ensemble average was introduced recently [3], and speeds up calculations for low-density systems considerably. Perturbation theory and integral-equation methods have also been used to connect a molecular model to its bulk dielectric constant, but these approaches are limited to relatively simple model systems.

At low concentration, the dielectric constant can be estimated via a power series in density, with coefficients expressed rigorously in terms of molecular interactions [4]. Although the requirement for low density can be a severe limitation, such approaches are generally not restricted to simple molecular models, because the coefficients are expressed as a configurational average that can be computed using methods similar to those employed by molecular simulation. Still, to date only low-order coefficients have been computed, and these for rather simple potentials. Hence, the performance of the series-based framework is not well explored.

To third order in density, the dielectric constant is given via the following expression [5, 6]:

$$\frac{\epsilon - 1}{\epsilon + 2} = A_\epsilon^* \rho^* + B_\epsilon^* \rho^{*2} + C_\epsilon^* \rho^{*3} + \dots, \tag{2}$$

where A_ϵ^*, B_ϵ^* and C_ϵ^* are the first, second and third dielectric virial coefficients, respectively, made dimensionless using a characteristic size σ, and likewise the dimensionless number density $\rho^* \equiv \rho\sigma^3$ with $\rho \equiv N/V$ for N molecules in a volume V; typically σ is taken as an atom diameter or potential parameter. When Eq. (2) is truncated after the first term, we recover the Clausius-Mossotti-Debye equation, for which

$$A_\epsilon^* = \frac{4\pi}{9}\beta^* \mu^{*2} + \frac{\alpha}{3\epsilon_0 \sigma^3}, \tag{3}$$

where μ and α are the molecular dipole moment and polarizability, respectively, and $\beta^* \equiv \varepsilon\beta \equiv \varepsilon/k_\mathrm{B}T$ with k_B Boltzmann's constant, T the temperature, while ε defines a unit of energy (not to be confused with the dielectric constant ϵ); $\mu^{*2} \equiv \mu^2/4\pi\epsilon_0\sigma^3\varepsilon$. Joslin [5] derived expressions for the second and third dielectric virial coefficients for a non-polarizable model, and Gray et al. [6] extended these to include molecular polarizability. We focus on non-polarizable models here, so we take $\alpha = 0$ in all that follows. Then, for a pairwise additive potential u_{ij}, the second and third dielectric virial coefficients are given as follows [5]:

$$B_\epsilon^* = \frac{4\pi}{9}\beta^* \mu^{*2} \left\langle \int \hat{\boldsymbol{\mu}}_1 \cdot \hat{\boldsymbol{\mu}}_2 e_{12} d\mathbf{r}_{12}^* \right\rangle_{\omega_1\omega_2} \tag{4}$$

$$C_\epsilon^* = \frac{4\pi}{9}\beta^* \mu^{*2} \left\langle \int \hat{\boldsymbol{\mu}}_2 \cdot \hat{\boldsymbol{\mu}}_3 f_{12} e_{23} f_{13} d\mathbf{r}_{12}^* d\mathbf{r}_{13}^* \right\rangle_{\omega_1\omega_2\omega_3} \tag{5}$$

where $\hat{\boldsymbol{\mu}} \equiv \boldsymbol{\mu}/\mu$ is a unit dipole vector, the subscripted angle brackets indicate an average over the orientations of each molecule, and

$$e_{ij} \equiv \exp(-\beta u_{ij}); \quad f_{ij} \equiv e_{ij} - 1. \tag{6}$$

The electric field $\mathbf{E}$ appearing in Eq. (1) differs from the applied field $\mathbf{E}_0$, i.e. the one that would be imposed in an experiment, or used as an independent variable in the thermodynamic formalism for dielectric materials. The field $\mathbf{E}$ includes contributions from the polarized dielectric itself, and the relation between $\mathbf{E}$ and $\mathbf{E}_0$ is made via classical electrostatics [2].

The right-hand side of Eq. (2) is derived via a statistical mechanical cluster expansion of the free energy [5]. Differentiation of the free-energy series with respect to $\mathbf{E}_0$ yields the polarization $\mathbf{P}$ in terms of $\mathbf{E}_0$. From this, a relation between $\mathbf{P}$ and $\mathbf{E}$ can be obtained, and the dielectric constant follows from Eq. (1). The extra steps needed to relate $\mathbf{E}$ to $\mathbf{E}_0$ lead to the slightly more complicated form involving ϵ appearing on the left-hand side of Eq. (2).

All of the foregoing development is based on the modeled system being embedded in a vacuum. More generally, the system may be embedded in a homogeneous dielectric having relative permittivity ϵ', and this will affect the formulas because the embedding medium too will contribute to the field $\mathbf{E}$ as it responds to the polarization $\mathbf{P}$. Typical choices are $\epsilon' = 1$, which corresponds to the vacuum; $\epsilon' = \infty$, the so-called "tin-foil" boundary; and $\epsilon' = \epsilon$, the self-consistent boundary, in which the modeled system is surrounded by a medium matching its own dielectric properties.

The left-hand side of Eq. (2) is modified for the presence of the embedding dielectric, again using classical electrostatics [2, 7]. The effect on the right-hand side is through the coefficients as given by Eqs. (4) and (5) (the A_ϵ^* term is not affected by the dielectric boundary). Each dipole in the modeled system contributes to the field experienced by the

surrounding medium, which responds with its own ϵ'-dependent "reaction field" which then interacts uniformly with every other molecular dipole in the system. The net result can be expressed as an effective pair interaction between the dipoles [2]:

$$\beta u_{ij}^{\mathrm{RF}}(r_{ij}) = \begin{cases} -\mathcal{R}_{\epsilon'}\beta^*\mu^{*2}\hat{\boldsymbol{\mu}}_i \cdot \hat{\boldsymbol{\mu}}_j / r_c^{*3}, & \text{for } r_{ij} \le r_c \\ 0, & \text{for } r_{ij} > r_c \end{cases} \tag{7a}$$

where $r_c^* = r_c/\sigma$ for the interaction cutoff radius r_c, and

$$\mathcal{R}_{\epsilon'} \equiv \frac{2(\epsilon'-1)}{2\epsilon'+1}. \tag{7b}$$

This effective interaction depends on the orientations of the dipoles, but not their separation distance (apart from the truncation at r_c). Equations (4) and (5) are modified by adding u_{ij}^{RF} to all pair interactions. These modifications can in fact be handled analytically, yielding expressions in terms of the coefficients A_ϵ^*, B_ϵ^* and C_ϵ^* as already defined by (3)-(5), so there is no need to introduce new ϵ'-dependent coefficients. These manipulations are demonstrated for B_ϵ^* in the Appendix.

The dielectric virial series for $\epsilon' = 1$ is given already by Eq. (2). For $\epsilon' = \infty$, the appropriate expression is:

$$\frac{\epsilon-1}{3} = A_\epsilon^*\rho^* + (B_\epsilon^* + A_\epsilon^{*2})\rho^{*2} + (C_\epsilon^* + 2A_\epsilon^*B_\epsilon^* + A_\epsilon^{*3})\rho^{*3} + \ldots, \tag{8}$$

while for $\epsilon' = \epsilon$, it is [8]:

$$\frac{(2\epsilon+1)(\epsilon-1)}{9\epsilon} = A_\epsilon^*\rho^* + B_\epsilon^*\rho^{*2} + \left(C_\epsilon^* + 2A_\epsilon^{*3}\right)\rho^{*3} + \ldots. \tag{9}$$

The choice $\epsilon' = \epsilon$ implies a density-dependent u_{ij}^{RF}, and consequently the contribution of the reaction field to B_ϵ^* is manifested instead in C_ϵ^* (and higher coefficients) [8, 9] (see Appendix).

Consistent with the fact that ϵ is a material property with value that is independent of the choice of the dielectric boundary, Eqs. (2), (8), and (9) all yield the same series when expressed in terms of ϵ directly, which to third order is:

$$\epsilon = 1 + 3A_\epsilon^*\rho^* + 3(B_\epsilon^* + A_\epsilon^{*2})\rho^{*2} + 3(C_\epsilon^* + 2A_\epsilon^*B_\epsilon^* + A_\epsilon^{*3})\rho^{*3} + \ldots \tag{10}$$

The leading correction term B_ϵ^* has been the subject of numerous studies. Buckingham and Joslin presented an analytical expression of B_ϵ^* for a dipolar hard-sphere fluid [10]. Later, Powles and McGrath [11], and Stone et al. [12] studied B_ϵ^* of HCl using several more realistic molecular models. One important feature of the models mentioned above is that the van der Waals interaction and the dipole interaction share one center. Dymond and Smith studied B_ϵ^* of off-center dipole models [13], where the center of the hard-sphere potential and center of the dipole potential are not superimposed.

Fewer attempts have been made to calculate C_ϵ^*. Since the dipole-dipole interaction is long ranged (decaying as $1/r^3$), the integral in Eq. (5) is conditionally convergent and therefore difficult to calculate. Early attempts to evaluate the integral were based on high-temperature/small-μ expansions [4, 5, 14, 15]. These approaches are not effective at every condition of interest, and the difficulty of evaluating additional expansion coefficients exceeds that of evaluating C_ϵ^* itself. For the special case of a dipolar hard-sphere fluid, Joslin and Goldman split the integral into two parts [8]:

$$C_\epsilon^* = C_\epsilon^{*(1)} + C_\epsilon^{*(2)} \tag{11a}$$

$$C_\epsilon^{*(1)} = \frac{4\pi}{9}\beta^*\mu^{*2}\left\langle \int \hat{\boldsymbol{\mu}}_2 \cdot \hat{\boldsymbol{\mu}}_3 f_{12}f_{23}f_{13}d\mathbf{r}_{12}^* d\mathbf{r}_{13}^* \right\rangle_{\omega_1,\omega_2,\omega_3} \tag{11b}$$

$$C_\epsilon^{*(2)} = \frac{4\pi}{9}\beta^*\mu^{*2}\left\langle \int \hat{\boldsymbol{\mu}}_2 \cdot \hat{\boldsymbol{\mu}}_3 f_{12}f_{13}d\mathbf{r}_{12}^* d\mathbf{r}_{13}^* \right\rangle_{\omega_1,\omega_2,\omega_3} \tag{11c}$$

The convergence difficulty is thereby isolated in $C_\epsilon^{*(2)}$. By applying a Taylor expansion to f_{ij} and employing some mathematical treatments, Joslin and Goldman developed an

expression of $C_\epsilon^{*(2)}$ for a dipolar hard-sphere fluid. They then evaluated C_ϵ^* for a wide range of dipole moments.

Very few experimental data are available for the third dielectric virial coefficient. Sutter and Cole measured C_ϵ^* for CHF_3 at various temperatures [16]. Joslin and Goldman compared their results of C_ϵ^* of a hard-sphere fluid assuming $\mu = 1.65$ D (5.50×10^{-30} C-m) and $\sigma = 0.342$ nm. They found the values are much smaller than the experimental data. They argued that the crudeness of the model, such as the neglect of the polarizability and the molecular shape, causes the deviation. To our knowledge, no one has calculated C_ϵ^* for other molecular models.

This work is organized as follows. In the next section, we propose a new method to calculate the second dielectric coefficient B_ϵ^* and the third dielectric coefficient C_ϵ^*, for a generic molecular model. In section 2.1 we briefly describe the molecular models we use, including a dipolar hard-sphere fluid, a Stockmayer fluid and TIP4P water [17], and follow this with discussion of computation techniques and details. In section 3, we present our results of the second and third dielectric coefficients of the three models. Finally the dielectric constants ϵ predicted from the virial series are shown and compared with simulation data. We conclude our work in section 4.

2. Methods, models and computation details

2.1. *Molecular models*

We examine three molecular models in this work: dipolar hard spheres (DHS); dipolar Lennard-Jones (DLJ), also known as the Stockmayer fluid [18]; and TIP4P water [19]. The first two of these are the usual hard-sphere (HS) and Lennard-Jones (LJ) models, respectively, plus a point dipole embedded in each atom center. The dipole-dipole interaction is

$$\beta u_{12}^{\mathrm{DD}} = \beta^* \mu^{*2} \left(\frac{\sigma}{r}\right)^3 \left(\hat{\boldsymbol{\mu}}_1 \cdot \hat{\boldsymbol{\mu}}_2 - 3(\hat{\boldsymbol{\mu}}_1 \cdot \hat{\mathbf{r}})(\hat{\boldsymbol{\mu}}_2 \cdot \hat{\mathbf{r}})\right), \tag{12}$$

where $r = |\mathbf{r}|$ is the distance between two molecules separated by the vector $\mathbf{r}$ from molecule 1 to molecule 2, and $\hat{\mathbf{r}}$ is the unit vector $\mathbf{r}/r$. The dipole magnitude μ is one of the model parameters investigated in this work. The second and third pressure virial coefficients of the DLJ model were recently reported by Elfimova et al. [20].

The TIP4P potential is a typical pairwise-additive model for water [19]. It features a LJ interaction located at the oxygen atom center, and three partial charges located at hydrogen atoms and an off-atom site, labeled "M". Bond length O-H is 0.9572 Å; distance O-M is 0.15 Å; the LJ σ and $\varepsilon/k_{\mathrm{B}}$ on oxygen are 3.1536 Å and 64.8694 K, respectively. Angle H-O-H is 104.52°, and partial charges on M and H are $q_M = -1.04e$ and $q_H = +0.52e$, respectively (where e is the charge of an electron). A hard core of 1.265 Å is imposed at the position of the oxygen atom to avoid the divergence of the Coulomb interactions if two molecules are very close. The equivalent dipole resulting from the three partial charges is located at the center of the charges (defined $\sum_i |q_i|\mathbf{r}_i / \sum_i |q_i|$), with orientation along the M-O axis. Its magnitude is $\mu = 2.177$ D, which corresponds to a reduced squared dipole moment of $\mu^{*2}\varepsilon/k_{\mathrm{B}} = 1094.5$ K (using $\sigma = 3.1536\mathring{A}$).

All models examined here are non-polarizable, i.e. the magnitudes of the dipoles and point charges are fixed.

2.2. *Second dielectric virial coefficient, B_ϵ*

For potentials in which the only anisotropic component is due to the dipole-dipole interaction, a closed-form expression for B_ϵ^* is available [6, 9, 21]:

$$B_\epsilon^* = 72 \left(\frac{4\pi}{9}\beta^*\mu^{*2}\right)^2 \sum_{n=1}^{\infty} \left(\beta^*\mu^{*2}\right)^{2n} \left(\frac{2^n(n+1)!}{(2n+3)!}\right)^2 J_{6n+3}(\beta) \sum_{t=0}^{n} \frac{(3t-n)(2t)!}{(t!)^2} \tag{13a}$$

with

$$J_k(\beta) = \sigma^{k-3} \int_0^\infty dr r^{2-k} \exp\left[-\beta u(r)\right]. \tag{13b}$$

Among the potentials of interest here, this formula can be applied to the dipolar hard-sphere (DHS) and Stockmayer (DLJ) models, for which

$$J_{6n+3}^{\mathrm{DHS}} = \frac{1}{6n} \tag{14}$$

and

$$J_{6n+3}^{\mathrm{DLJ}} = \frac{1}{12}\frac{1}{2^n}\frac{1}{\beta^{*n/2}}\left[\Gamma\left(\frac{n}{2}\right)\,{}_1F_1\left(\frac{n}{2};\frac{1}{2};\beta^*\right) + 2\beta^{*1/2}\Gamma\left(\frac{n+1}{2}\right)\,{}_1F_1\left(\frac{n+1}{2};\frac{3}{2};\beta^*\right)\right] \tag{15}$$

where Γ is the Gamma function and ${}_1F_1$ is the Kummer confluent hypergeometric function.

For non-spherical potentials, Mayer sampling or another stochastic quadrature method can be an effective approach to evaluation of the B_ϵ integral. However, the long-range nature of the electrostatic interactions complicates a direct application of such methods. To remedy this problem, we look for ways to attenuate the interactions by introducing offsetting terms having contributions that can be subsequently removed analytically. The strategy we prefer is to evaluate the target integral after subtraction of the interaction for a solvable model having the same dipole moment; DHS provides a convenient choice. In this manner we cancel out the target-system dipole interaction at larger separations. The working equations are, thus:

$$\Delta B_\epsilon^* = \frac{4\pi}{9}\beta^*\mu^{*2}\left\langle \int \hat{\boldsymbol{\mu}}_1\cdot\hat{\boldsymbol{\mu}}_2(e_{12}-e_{12}^{\mathrm{DHS}})d\mathbf{r}_{12}^*\right\rangle_{\omega_1,\omega_2} \tag{16a}$$

$$B_\epsilon^* = \Delta B_\epsilon^* + B_\epsilon^{*\mathrm{DHS}} \tag{16b}$$

The integral in Eq. (16a) is absolutely convergent and can be evaluated via any of several quadrature methods. The desired coefficient B_ϵ^* is recovered using the expression for $B_\epsilon^{*\mathrm{DHS}}$ given by Eqs. (13) and (14).

2.3. *Third dielectric virial coefficient, C_ϵ*

We adopt Joslin and Goldman's treatment for C_ϵ^* (Eq. (11)) [8]. The problematic term, $C_\epsilon^{*(2)}$, is treated by adding $e_{ij}^0\beta u_{ij}^{\mathrm{DD}}$ to each f_{ij} function:

$$C_\epsilon^{*(2')} = \frac{4\pi}{9}\beta^*\mu^{*2}\left\langle \int \boldsymbol{\mu}_2\cdot\boldsymbol{\mu}_3\left(f_{12}+e_{12}^0\beta u_{12}^{\mathrm{DD}}\right)\left(f_{13}+e_{13}^0\beta u_{13}^{\mathrm{DD}}\right)d\mathbf{r}_{12}^*d\mathbf{r}_{13}^*\right\rangle_{\omega_1,\omega_2,\omega_3} \tag{17}$$

In Eq. (17), $e_{ij}^0=\exp(-\beta u_{ij}^0)$; u_{ij}^{DD} is the dipole-dipole potential energy (Eq. (12)) of the molecular pair i and j, and u_{ij}^0 is a spherically symmetric non-electrostatic potential between them, positioned at the same center as u_{ij}^{DD}. If the electrostatic energy of a fluid is represented by partial charges instead of point dipoles, such as the case for TIP4P water, then u_{ij}^{DD} is considered to be the equivalent dipole at the electrostatic center of the partial charges. In the present work, for TIP4P water we use the O-atom LJ potential for u_{ij}^0, but shifted to the center of charge so it is coincident with the effective dipole. A development is given in the Appendix to show that $C_\epsilon^{*(2)}$ and $C_\epsilon^{*(2')}$ are equal.

2.4. *Dielectric constant from simulation*

The development and study of methods for calculation of the dielectic constant by molecular simulation is a topic of continuing interest. Recent studies have examined the merits of fluctuation-analysis versus field-response formulations [22], and fixed-field versus fixed-displacement methods [23]. For most of our purposes, methods based on fluctuation formulas are suitable, although for low-density studies we turn to a recently developed mapped-averaging approach, which offers exquisite precision in this regime [3].

We apply Monte Carlo simulations in the canonical (NVT) ensemble to calculate the dielectric constant ϵ, and use the simulation data as a standard to assess the accuracy of the VEOS. We employ the reaction field method to treat long-range electrostatic interactions [1, 6], which is implemented by adding u_{ij}^{RF} (Eq. (7)) to the pair interactions. Then the working equation to calculate the dielectric constant is [2]:

$$\frac{\epsilon-1}{\epsilon+2}\left[1-\frac{\epsilon-1}{\epsilon+2}\quad\frac{2(\epsilon'-1)}{2\epsilon'+1}\right]^{-1} = \frac{4\pi}{9}\frac{\langle M^2\rangle}{k_{\mathrm{B}}TV} \tag{18}$$

where $\langle M^2 \rangle$ is the ensemble-averaged mean squared dipole moment in the simulation cell. As indicated by Neumann [2], the most accurate results of ϵ are obtained for $\epsilon' \geq \epsilon$. We use ϵ' given by Eq. (10) evaluated at third order using our values of the dielectric virial coefficients. As we see below, this form generally tracks well with the correct ϵ at each density, so it yields a suitable estimate to use for ϵ'. We also perform some simulations using the tin-foil boundary to check that the choice of ϵ' is not distorting the results.

2.5. *Computation details*

We apply Mayer sampling Monte Carlo (MSMC) [24] to evaluate all the integrals required for the dielectric virial coefficients. MSMC has been applied to virial coefficient calculations for a variety of potentials — including water [25–28] — but never for calculation of dielectric properties. It is based on ideas from free-energy perturbation methods, where the configuration integrals (such as virial coefficients) can be formulated as ratios of ensemble averages with sampling weights. To compute the value of an integral Γ, a reference integral Γ_0, such as for a hard sphere system, is required. The overlap-sampling implementation of MSMC [27, 28] is the most robust and effective approach. The working equation is

$$\Gamma = \Gamma_0 \frac{\langle \gamma/|\gamma| \rangle_{|\gamma|} / \langle \gamma_{\rm OS}/|\gamma| \rangle_{|\gamma|}}{\langle \gamma_0/|\gamma_0| \rangle_{|\gamma_0|} / \langle \gamma_{\rm OS}/|\gamma_0| \rangle_{|\gamma_0|}}, \tag{19a}$$

where

$$\gamma_{\rm OS} = \frac{|\gamma||\gamma_0|}{|\gamma_0| + \alpha_{\rm OS}|\gamma|} \tag{19b}$$

In this expression, $|\gamma|$ is the absolute value of the target integrand, and $|\gamma_0|$ is the absolute value of the reference integrand. Two Markov chains are employed: the numerator on the right-hand side in Eq. (19a) is one with a sampling weight taken to be $|\gamma|$, and the denominator is one with a sampling weight taken to be $|\gamma_0|$. $\gamma_{\rm OS}$ (overlap) is the integrand for a hybrid system having configurations important to the both target and reference systems. $\alpha_{\rm OS}$ is optimized prior to data collection. More details are available in Refs. [27, 28].

Computation of the coefficients requires a hard sphere model as the reference (it need not be dipolar). In principle, the choice of the hard sphere size of the reference is arbitrary, but it is reasonable and convenient to choose the hard sphere size to be characteristic of the range of interaction. We use a reference hard-sphere diameter equal to 2σ for calculation of C^*_ϵ(DHS) and B^*_ϵ(DLJ), and 4σ for calculation of C^*_ϵ(DLJ), where σ here is the HS or LJ diameter of the target system; for TIP4P water, the diameter of hard sphere reference system is 7.0 $\mathring{A}$ for calculation of all coefficients.

For each configuration during the B_ϵ calculation, we build a dipolar hard sphere for use in Eq. (16a) as follows: the hard sphere atom is put at the position of the dipole of the target molecule, or the equivalent dipole in the case of TIP4P water. The dipole strength and orientation are set equal to those of the target molecule in the current configuration.

No special technique is needed when we evaluate $C^{*(1)}_\epsilon$. To evaluate $C^{*(2')}_\epsilon$, we calculate f_{ij} directly from molecular models. For DHS, u^0_{ij} is simply the hard-sphere potential, and for the Stockmayer fluid or TIP4P water it is the simple LJ interaction. The interaction site of u^0_{ij} is on the center of the dipole or the corresponding dipole. For TIP4P water, the position of the corresponding point dipole is located as described in Sec. 2.1. Also, $u^{\rm DD}_{ij}$ for TIP4P water is calculated from Eq. (12), not from summing Coulomb's law over the pairs of point charges.

We run 10 (20 for TIP4P water B_ϵ) independent MSMC calculations with 10^9 Monte Carlo steps for each dielectric virial coefficient, and each run is separated into 1000 10^6-step blocks that are subaveraged for error analysis. About 1% to 5% of the steps are spent on sampling the hard-sphere reference, with the remainder spent on the target system. Data from all blocks from all runs are collected to compute the four averages appearing in Eq. (19). The fluctuations in the blocks are analyzed, and with proper attention to the correlation between the blocks the results are propagated to the calculation of the uncertainty in the coefficient, reported here at the 68% confidence level.

In the Monte Carlo simulations, we set r_c, the cutoff distance for all interactions, to be half of the length of the simulation box. We run simulations of DHS with 100, 200, and 400 molecules, the Stockmayer fluid for 100 and 200 molecules, and TIP4P water using 256 molecules. Each simulation has 10^8 Monte Carlo steps, collected into 100 blocks for DHS, and 1000 blocks for DLJ and TIP4P water, which are used for error analysis (the blocks are found to yield statistically uncorrelated averages). The first 20% of sampling is for equilibrating, and the averages of M^2 are taken after the equilibration finishes. For TIP4P water, the dielectric constant is computed by averaging M^2 across 10 independent simulations according to Eq. (18). For DHS, the dielectric constant is computed with mapped averaging employing 20 simulations for densities up to $\rho^* = 0.1$ and 2 simulations for higher densities. For DLJ, 10 mapped averaging simulations are used for each density.

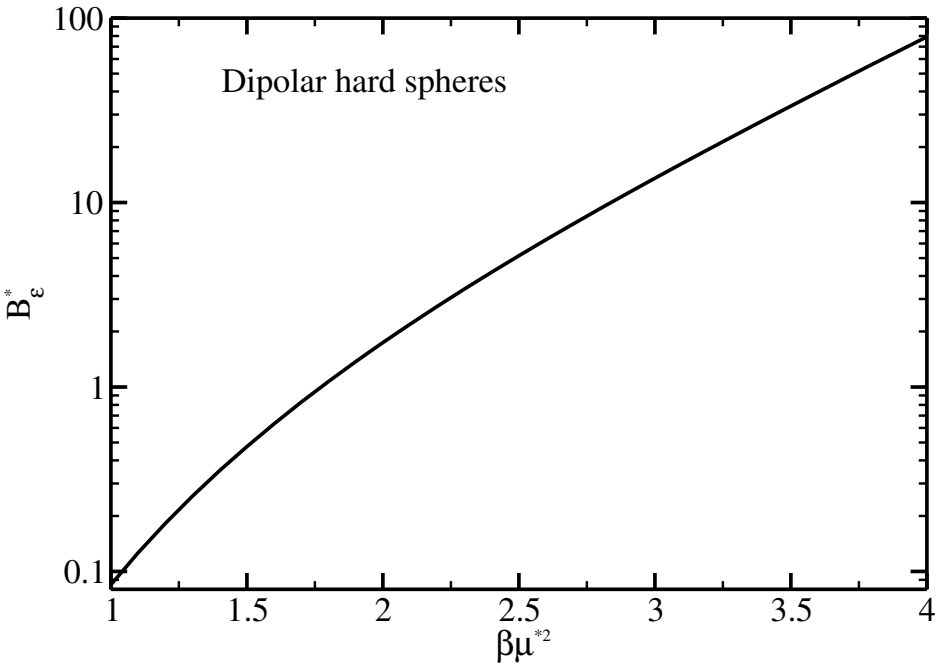

Figure 1. Reduced second dielectric virial coefficient B_ϵ^* as a function of the reduced dipole strength $\beta^*\mu^{*2}$ for the dipolar hard-sphere model. Values are given by numerical summation of Eq. (13) with Eq. (14).

For each model and state, data from all blocks from all independent simulations are collected to compute uncertainties, which represent 68% confidence intervals.

3. Results and discussion

3.1. *Virial coefficients*

Figure 1 presents B_ϵ^* for the DHS model, plotted over most of the range of $\beta^*\mu^{*2}$ values that we examine in this work. This is simply a graphical representation of Eqs. (13) and (14), and we present it because this quantity enters into the calculation and presentation of other results to follow below. We note that B_ϵ^* increases monotonically with $\beta^*\mu^{*2}$, reflecting the increased susceptibility of the system to an electric field as μ increases relative to T. The value of B_ϵ^* varies across four orders of magnitude as $\beta^*\mu^{*2}$ ranges from 1 to 4.

To demonstrate the correctness and effectiveness of the approach for computing C_ϵ^*, we present results for dipolar hard spheres, computed according to Eqs. (11) and (17) via MSMC. Joslin and Goldman [8] reported the same results using the same breakdown into $C_\epsilon^{*(1)}$ and $C_\epsilon^{*(2)}$ but with a different numerical technique, not involving Eq. (17), so these provide a good basis for validation of the new approach. Results are shown in Fig. 2. The raw C_ϵ^* data range over several orders of magnitude, but a log plot is not suitable because they encompass both positive and negative values. Instead, the data are reduced by B_ϵ^* (not B_ϵ^{*2} as is the usual practice for the pressure virial coefficients) of DHS for the same $\beta^*\mu^{*2}$, which puts all values at the same magnitude. Excellent agreement can been seen between the present results and the literature values; the new data have better precision as well. All new data are tabulated in the Supplemental Information.

Turning now to the Stockmayer model, Figs. 3 and 4 respectively show the reduced second and third dielectric virial coefficients, B_ϵ^* and C_ϵ^*. The second dielectric virial B_ϵ^* can be computed exactly via Eqs. (13) and (15), and we can use these values to demonstrate that we obtain correct results via the MSMC calculation of ΔB_ϵ^* according to Eq. (16). While the Stockmayer coefficient B_ϵ^*(DLJ) varies over several orders of magnitude for the range of $\beta^*\mu^{*2}$ examined, it is roughly proportional to B_ϵ^*(DHS) (for the same $\beta^*\mu^{*2}$) across the entire range, so we present the results as reduced by the DHS value. Figure 3 indeed shows perfect correspondence between the MSMC results and the exact values. The ratio B_ϵ^*(DLJ)/B_ϵ^*(DHS) is greater than unity for all conditions, showing that the Lennard-Jones attraction leads to general clustering of the particles, and a consequent increase in their cooperative response to an external field (and thus a greater dielectric constant). The proportionality initially decreases with increasing temperature (for fixed $\beta^*\mu^{*2}$), reflecting the relative loss of importance of the LJ attraction; it then increases again, which is likely a manifestation of the softer LJ core allowing the dipole pairs to access closer separations than available to the DHS system.

The third dielectric virial coefficient for the Stockmayer model is presented in Fig. 4 in terms of its ratio with B_ϵ^*(DLJ), as was done for the DHS C_ϵ^*. The contribution to C_ϵ^* from

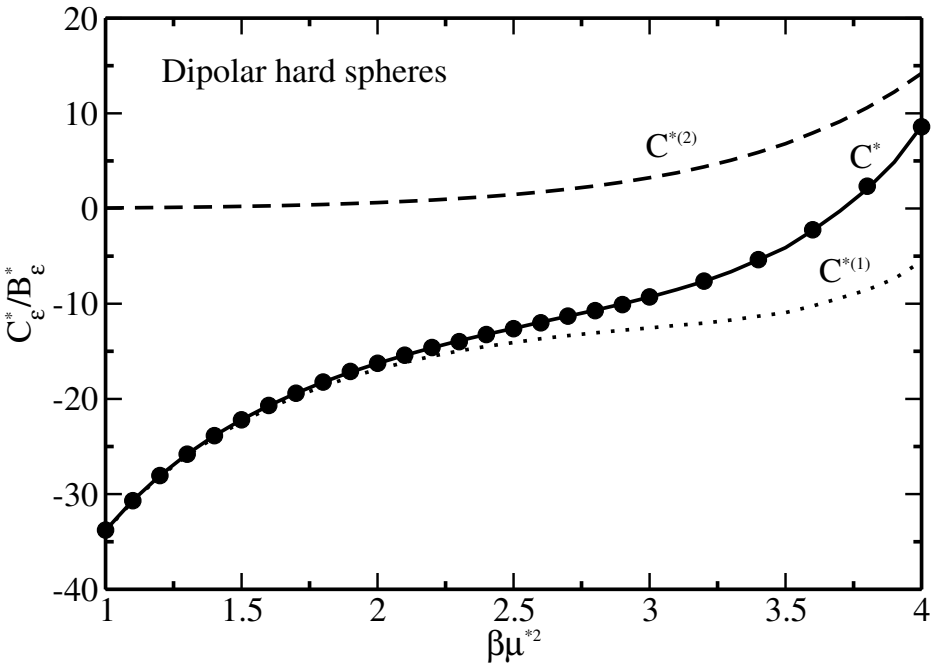

Figure 2. Reduced third dielectric virial coefficient C_ϵ^* as a function of reduced dipole strength $\beta^*\mu^{*2}$. To provide a better scale for presentation, values are divided by the reduced second-order coefficient B_ϵ^* (Fig. 1) for DHS at the same $\beta^*\mu^{*2}$. Labels next to the lines indicate the component of the coefficient as defined in Eq. (11). Lines are from the present calculations, and join 31 independent MSMC results, with uncertainties smaller than the line thickness. Circles are the results reported by Joslin and Goldman [8].

$C_\epsilon^{*(1)}$ dominates for $\beta^*\mu^{*2}$ less than about 2.5, where contributions from $C_\epsilon^{*(2)}$ start to become significant. The general behavior is similar to that for C_ϵ^* for DHS, although the magnitude of the DLJ coefficient is somewhat larger, more so with decreasing temperature (for fixed $\beta^*\mu^{*2}$).

The TIP4P potential is a much more realistic molecular model compared to the DHS and DLJ fluids, and it differs from them in that it models its electrostatic features with partial charges rather than a point dipole. Figure 5 displays both the second and third dielectric virial coefficients of TIP4P water from 250 K to 1000 K. B_ϵ^* is positive and C_ϵ^* is negative over the entire temperature range under consideration, so we present them together as B_ϵ^* and $-C_\epsilon^*$ using a log scale. The B_ϵ^*(TIP4P) curve has a similar shape to the B_ϵ^*(DHS) curve, which is presented on the plot for comparison. We see that B_ϵ^*(DHS) $> B_\epsilon^*$(TIP4P) for all but the largest values of $\beta^*\mu^{*2}$, which is contrary to what is seen for DLJ, where B_ϵ^*(DHS) $< B_\epsilon^*$(DLJ) for all conditions examined.

Turning briefly to C_ϵ^*, we note that it does not scale as well with respect to B_ϵ^* as did the DHS and DLJ models, so we have not presented it as in Figs. 2 and 4. A notable feature in the curve is a kink at about $\beta^*\mu^{*2} = 2$. This is in the vicinity of the critical temperature, but this connection is most likely a coincidence.

3.2. *Prediction of dielectric constants*

We now turn to consideration of the ability of the third-order dielectric virial series to estimate the bulk dielectric constant. Given a set of coefficients, $A_\epsilon^*, B_\epsilon^*$, etc., the dielectric constant can be estimated by solving for it in series for the vacuum dielectric boundary ($\epsilon' = 1$, Eq. (2)), the tin-foil boundary ($\epsilon' = \infty$, Eq. (8)), or the density-dependent self-consistent boundary ($\epsilon' = \epsilon$, Eq. (9)).

Let us look at all of these in relation to the DHS model. Figure 6 presents the estimates of ϵ given by all three forms, as a function of density and showing the progression as higher-order coefficients are included for each case; plots are shown both for $\beta^*\mu^{*2}$ equal to 1.0 and 2.0. The figure includes panels describing behavior over the full range of density examined here, and others showing zoomed-in views of the low-density behavior, dividing by ρ^2 to further amplify any differences (in this form, the VEOS1 difference has a non-zero intercept). The first point to notice is the considerable variation in the performance of the three boundary-dependent formulations. The form based on the vacuum boundary, $\epsilon' = 1$, diverges sooner as the density is increased, and it does so more severely. This behavior contrasts with that based on the tin-foil boundary, which is the opposite extreme with $\epsilon' = \infty$. Here both VEOS2 and VEOS3 track the simulation data quite well over the whole range of densities, staying at least qualitatively correct at higher densities. The performance for the intermediate case, $\epsilon' = \epsilon$, lies between that for the extremes of $\epsilon' = 1$ and ∞. The overall behavior of the VEOS formulations is consistent with observations about the effect of

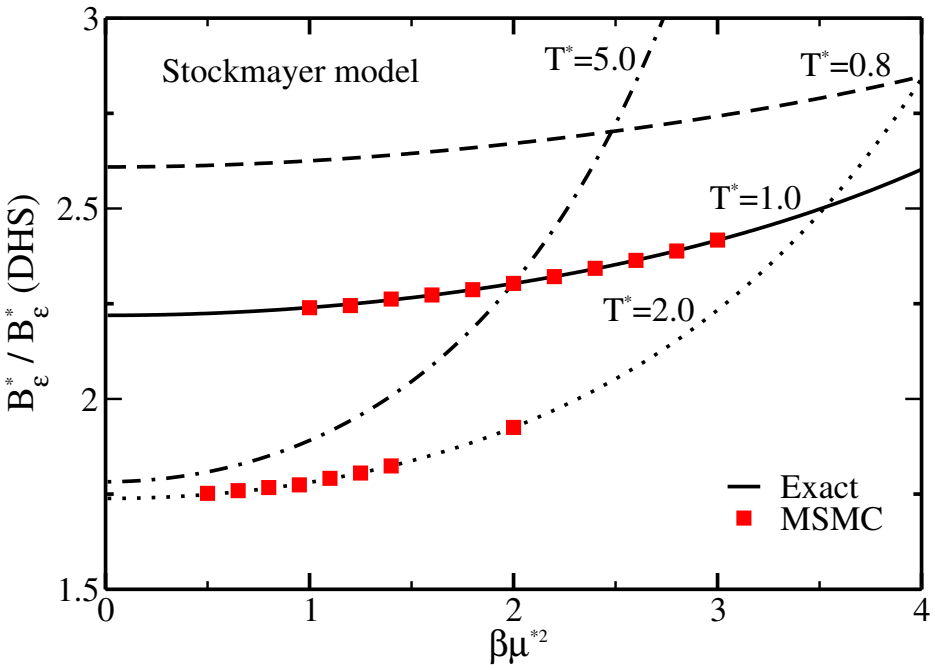

Figure 3. Reduced second dielectric virial coefficient B_ϵ^* of the Stockmayer fluid, divided by the value for dipolar hard spheres with the same $\beta^*\mu^{*2}$. Lines are computed for the indicated temperatures by numerical summation of Eq. (13) with Eq. (15). Points are from MSMC calculations applied to Eq. (16), which were performed only for the two temperatures $T^* = 1.0$ and 2.0. All uncertainties are smaller than the symbol sizes.

ϵ' on molecular simulations that use the reaction field, wherein poor results are obtained when $\epsilon' \ll \epsilon$, but the use of $\epsilon' \gg \epsilon$ is usually not detrimental to the results (however we will shortly provide a counterexample).

The simulations here employed an ϵ' given by the third-order form of Eq. (9) and we see that system size N does not have a large effect on the simulation data (the erratic dependence on N for $\beta^*\mu^{*2} = 2$ at $\rho^* = 0.9$ may be indicative of a phase transition). Not surprisingly, the dielectric VEOS overall performs better for the system having smaller dipolar coupling strength $\beta^*\mu^{*2}$.

Turning now to the Stockmayer fluid, we will focus attention on $T^* \equiv \beta^{*-1} = 2.0$. The other temperature where we have coefficient data, $T^* = 1.0$ is subcritical, and the dielectric virial series can be applied only to the relatively low densities below the spinodal, where we find it provides an excellent description of the dielectric constant (not shown). Kriebel and Winkelmann [29] report that the Stockmayer fluid at $T^* = 2.0$ is supercritical for dipole strength μ^{*2} up to at least 3.0, corresponding to $\beta^*\mu^{*2}$ less than about 1.5. Accordingly, Fig. 7 shows $T^* = 2.0$ isotherms of the dielectric constants for DLJ having $\beta\mu^{*2}$=0.5 and $\beta\mu^{*2}$=1.5, presented in the same manner as for DHS in Fig. 6. Each plot compares to simulation data the dielectric series to various orders, using the three choices of ϵ' described above. The behavior is very similar to that observed in application to DHS. Clearly the vacuum boundary yields a poor description of the simulation data, while the relative performance of the other two choices is mixed: the tin-foil boundary is better all-around when truncated at VEOS2, while for truncation at VEOS3 the relative performance of the self-consistent and tin-foil boundaries varies in no systematic manner for low versus high density and smaller versus larger $\beta^*\mu^{*2}$. Both choices remain reasonably close to the simulation data at all conditions.

For this model we computed simulation data for two choices of the reaction-field dielectric constant. One set of data (open symbols) shows results for the tin-foil boundary, and the other (filled symbols) shows results for using the self-consistent boundary. At low density there is a very clear effect on the computed dielectric constant, with the tin-foil boundary yielding results that are clearly inaccurate. Such an outcome is understandable, because at such low densities ϵ is nearly that of the vacuum, hence when surrounding it by a tin-foil dielectric we introduce a considerable finite-size effect. In this regard we note that the low-density $\epsilon' = \infty$ data move toward the other data (and the VEOS description) when the system size is increased. On the other hand, we should point out that the inaccuracy is evident only because of the way the data are presented, being differenced from VEOS3 and divided by ρ^2. The plots not scaled this way, and showing results for the full density range, do not exhibit an appreciable affect of the choice of ϵ' on the simulation data (we did not do simulations using the vacuum boundary, and we anticipate that they would not provide results with the same accuracy at the higher densities).

Finally, we compute the dielectric constants of TIP4P water at three temperatures. We use MC simulation data and a density-temperature correlation as references [30]. The latter provides a surrogate for experimental behavior, and we should expect to find disagreement

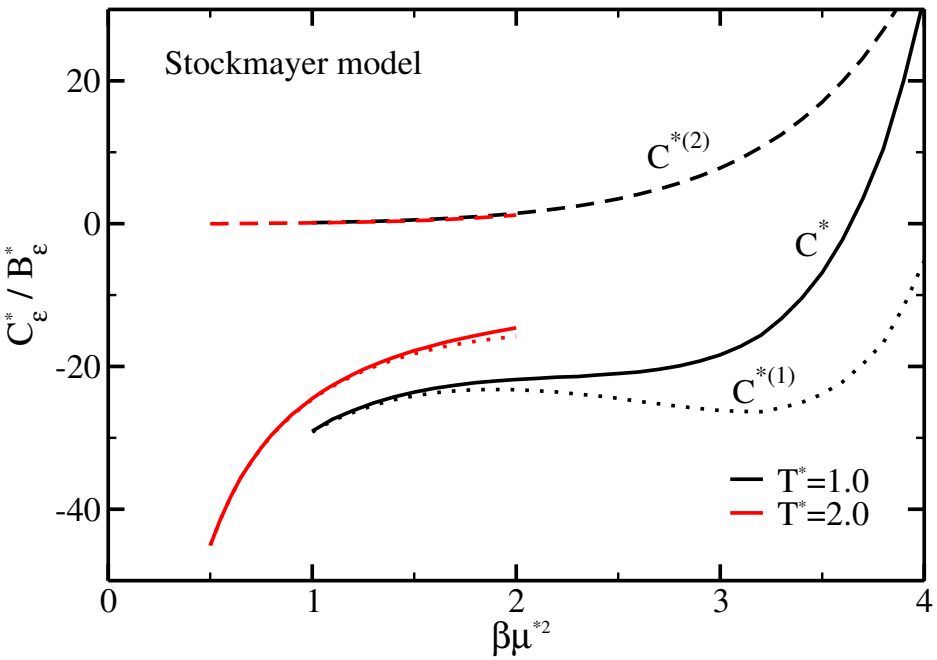

Figure 4. Reduced third dielectric virial coefficient C^*_ϵ of the Stockmayer fluid at $T^* = 1.0$ and 2.0 respectively, relative to the reduced second dielectric virial coefficient for the same conditions and model. Labels next to the lines indicate the component of the coefficient as defined in Eq. (11). Lines are from the present calculations, and join 31 independent MSMC results, with uncertainties smaller than the line thickness. Red lines for $T^* = 2.0$ range from $\beta^*\mu^{*2} = 0.5$ to 2.0.

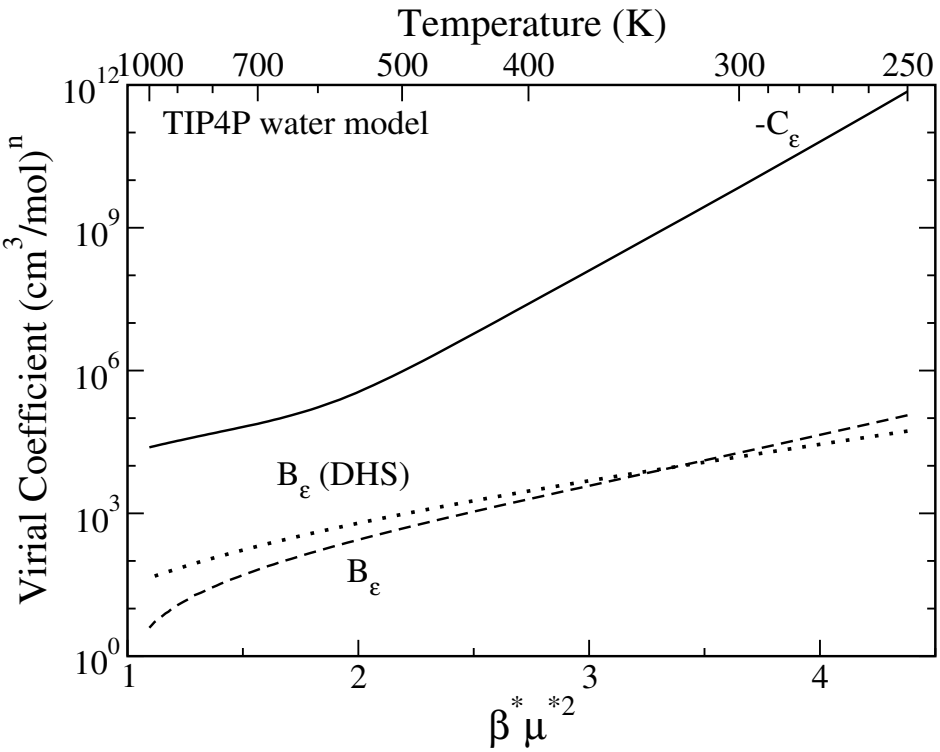

Figure 5. Second and third dielectric virial coefficients of TIP4P water from 250 K to 1000 K. Top-axis scale indicates the temperature corresponding to the $\beta^*\mu^{*2}$ values on the bottom axis, using $\mu^{*2}\varepsilon/k_B = 1094.5$ K. Lines connect 78 coefficient values computed by MSMC, with uncertainties smaller than the line thickness.

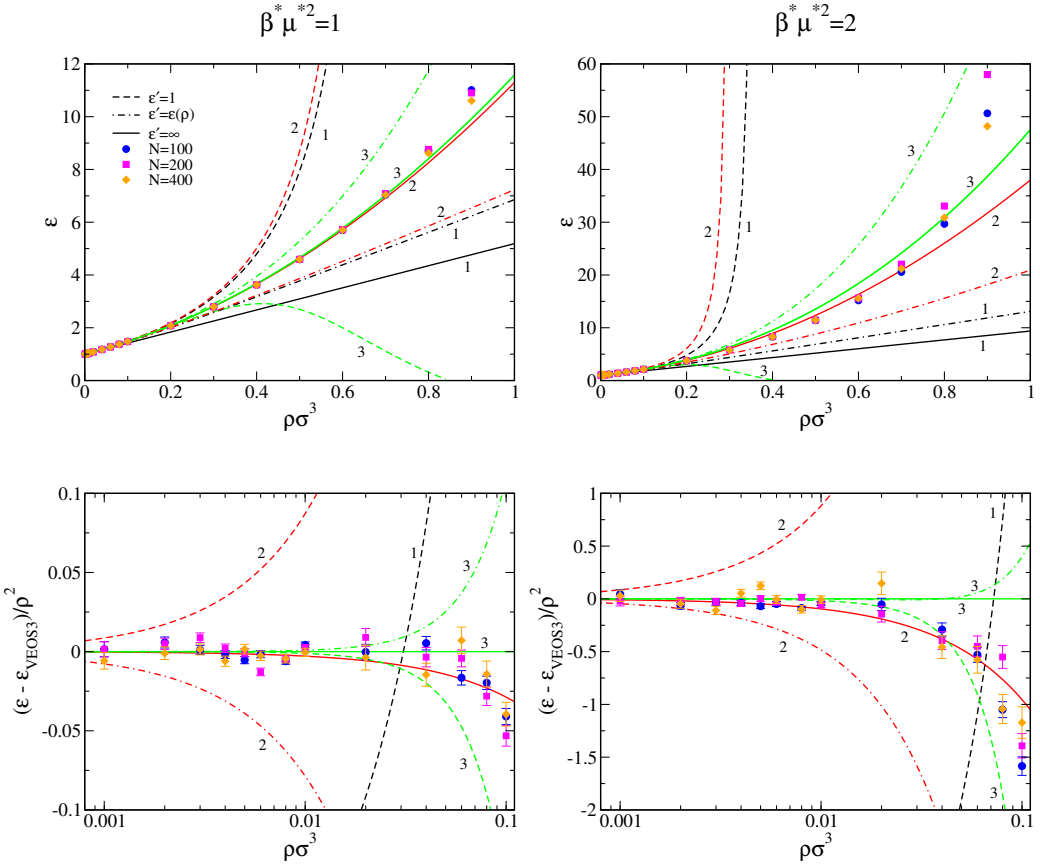

Figure 6. Dielectric constant for DHS fluid computed from the dielectric virial series. Left and right columns correspond to indicated values of $\beta^*\mu^{*2}$. The top row shows the absolute ϵ, while the bottom row shows the difference from ϵ for VEOS3 as given for the tin-foil boundary (Eq. (8)), with focus on low-density behavior (note the log scale). Line styles distinguish the different forms of the VEOS used to compute ϵ, as indicated in the legend: $\epsilon' = 1$, Eq. (2); $\epsilon' = \epsilon$, Eq. (9); $\epsilon' = \infty$, Eq. (8); numerals indicate the order of the series represented by the lines (which are also colored as: VEOS1, black; VEOS2, red; VEOS3, green). Points are results of molecular simulations performed for this study, using three system sizes as indicated by the legend; uncertainties (68% confidence) are shown only where larger than the symbols. Uncertainties in VEOS lines are smaller than line thickness.

with the dielectric constant given by the TIP4P model: the dipole moment of water in the gas phase is 1.85 D, and this is considerably less than the fixed value of 2.177 D for TIP4P, which results from fitting to condensed-phase data. A good description of the true dielectric behavior of water should use a polarizable model (which then requires including polarization in the calculation of the dielectric virial coefficients), or perhaps one that is parameterized to match ab initio potential data. For the present purpose, the performance of the dielectric virial series should be judged in comparison to the simulation data, which are computed for the same model.

Figs. 8 and 9 show the TIP4P dielectric constant as a function of density at 500 K, where TIP4P water is subcritical (its critical temperature is 588.2 K [31]). The spinodal density of water at 500 K is 0.73 mol/L [32], so the highest density examined here is 0.7 mol/L to keep the system in its stable gaseous state (to provide a scale, we note that the critical density for TIP4P water is 17.5 mol/L [31]). The simulation results for the two choices of the reaction-field ϵ' are in good mutual agreement, and as expected, they both give dielectric constants significantly larger than shown by the correlation. Compared to the simulation data, VEOS1 predicts the dielectric constants of TIP4P water to good accuracy over the full range of densities shown here, while VEOS2 and VEOS3 provide the slight adjustment needed to bring the series into excellent agreement with the simulation values. The more detailed comparison provided by the expanded-scale difference plot, Fig. 9, is not so conclusive about which choice of ϵ' for the virial series performs best in relation to simulation, because the forms differ from each other by less than the uncertainty in the simulation data. It is clear however that at this level, VEOS3 improves on VEOS2, which itself is marginally better than VEOS1 over this (low) density range.

Figures 10 and 11 look at the behavior of TIP4P ϵ for two supercritical temperatures: 680 K and 800 K, respectively. For these cases, the correlation is in reasonable agreement with MC data. As seen with the other models, estimates of ϵ obtained from VEOS using the vacuum-boundary formulation fail at intermediate densities; VEOS using the self-consistent boundary is qualitatively accurate, while VEOS with the tin-foil boundary is in

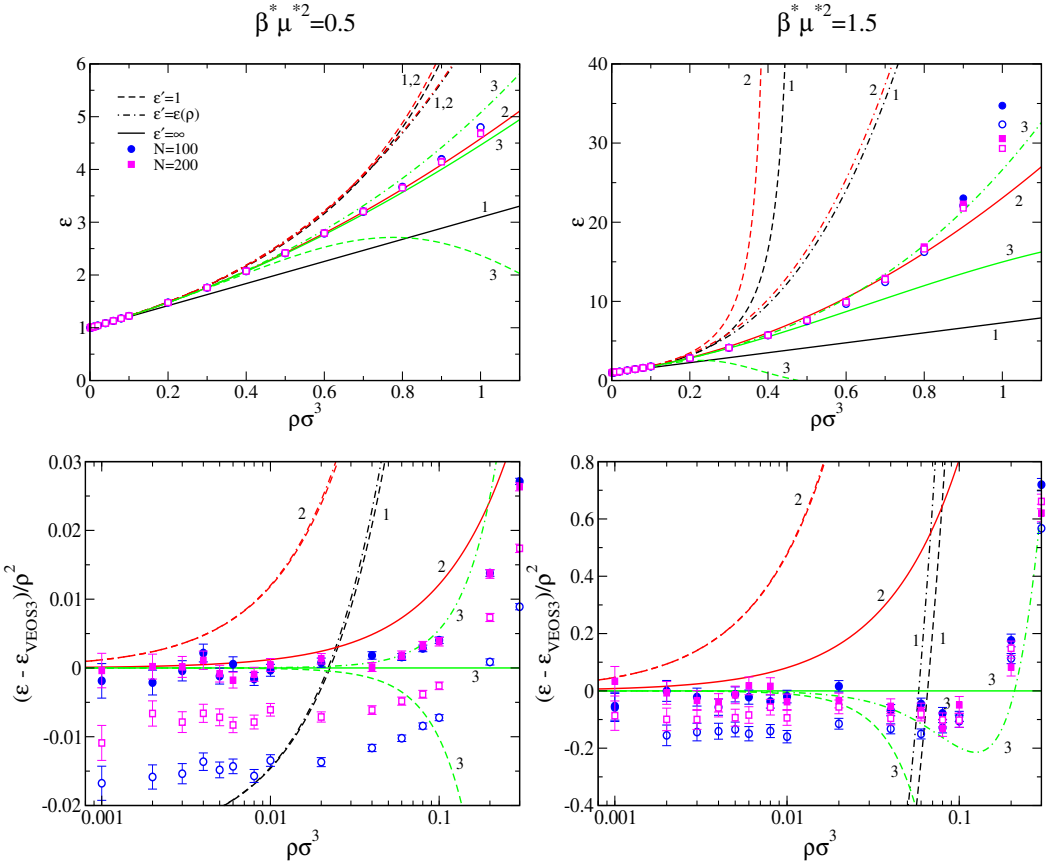

Figure 7. Dielectric constant ϵ for the DLJ fluid, $T^* = 2.0$, for two values of the relative dipole strength, as indicated above each column of plots. Points are results of molecular simulation, performed with reaction field $\epsilon' = \infty$ (open symbols) or the value given by VEOS3 as expressed in Eq. (10) (filled symbols); circles and squares distinguish simulation results for the two system sizes indicated in the legend. Other features of plots are as in Fig. 6. Note that the VEOS2 curves for $\epsilon' = \epsilon$ and $\epsilon' = 1$ are almost indistinguishable in both low-density plots.

near-quantitative agreement, even at 2nd order. The application considers densities up to about 10% above the critical, and the largest deviation of VEOS2 from simulation is about 7% of $\epsilon - 1$. The third-order term has a negligible effect.

4. Conclusion

We have demonstrated how the second and third dielectric virial coefficients of a general nonpolarizable molecular model can be computed. Such calculations are problematic due to the long-range nature of the electrostatic potentials, which are attenuated only upon averaging over the orientations of the molecules. This leads the relevant integrals to be conditionally convergent, requiring that integrations be performed in a specific order in the context of a well-defined limiting process. Such requirements can cause stochastic quadrature methods based on simple importance sampling to fail. To remedy this for the calculation of the third-order dielectric virial coefficient, we applied a strategy that has been successful previously in handling these systems: we subtract the problematic element from the integrals, isolating it into a simplified context that can be treated explicitly. The residual integral that remains is well-behaved and can be treated using otherwise-conventional methods (such as Mayer-sampling Monte Carlo). In this manner, we calculated coefficients up to third order in density and compared with simulation data the dielectric constants ϵ for three models: a dipolar hard-sphere fluid, a Stockmayer fluid and TIP4P water.

The dielectric virial series is derived in the context of an embedding dielectric, and the form of the series differs with the choice of the dielectric constant (ϵ') of the embedding medium. The vacuum boundary ($\epsilon' = 1$) yields the form given by Eq. (2); the self-consistent boundary ($\epsilon' = \epsilon$) yields Eq. (9); the tin-foil boundary ($\epsilon' = \infty$) yields Eq. (8). All of these forms are mutually consistent, such than when solved for ϵ and expanded in ρ they all yield Eq. (10) to third order. The quality of the description of ϵ differs considerably with the choice of ϵ', and we generally find that the tin-foil formulation yields the most accurate and reliable results (even when truncated at second order), while the vacuum boundary consistently fails except at the lowest densities.

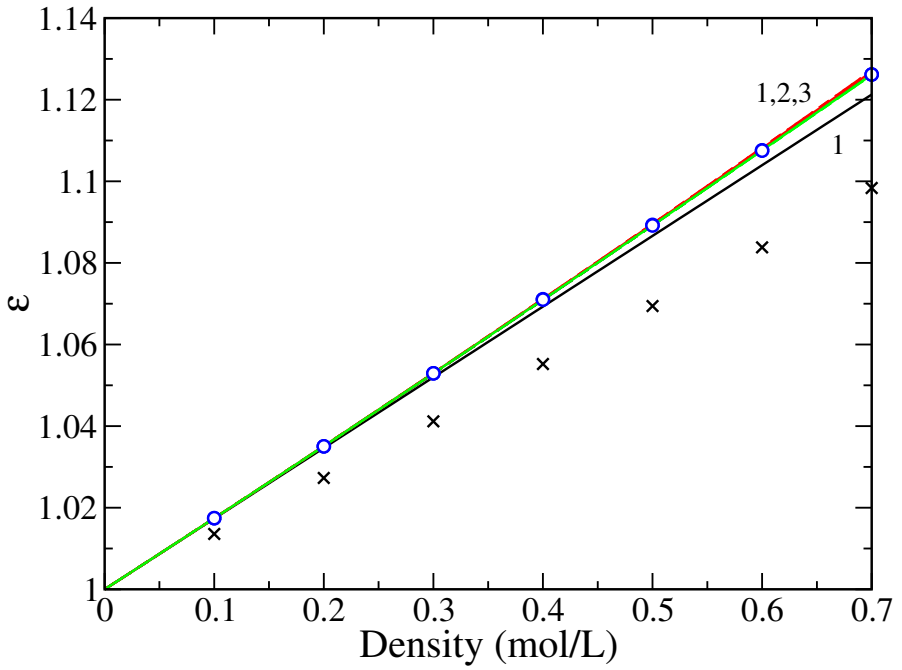

Figure 8. Dielectric constant ϵ of TIP4P water at 500 K ($\beta^*\mu^{*2} = 2.19$). Filled points are results of molecular simulation, with reaction field $\epsilon' = \infty$ (open circles) or the value given by VEOS3 (filled circles) (these two cases are indistinguishable on the plot); $\times$ symbols represent values for real water, as given by a correlation [30]. Lines are VEOS, with different styles indicating the different choices of the boundary dielectric ϵ', as specified in Figs. 6 and 7; numerals next to each line indicate the VEOS order. All lines except VEOS1 are indistinguishable on this scale.

A Supplemental Information file accompanies this paper. In it, we tabulate all values and uncertainties of the second and third dielectric virial coefficients computed for this work, and all values and uncertainties of the dielectric constant that we computed by molecular simulation.

Acknowledgments

Funding for this work was provided by the U.S. National Science Foundation, grants CHE-1027963 and CHE-1464581. Computational resources were provided by the University at Buffalo Center for Computational Research. We thank Weisong Lin for providing mapped-averaging data for the dielectric constant of the dipolar hard-sphere model.

5. Appendix

5.1. *Equivalence of $C_\epsilon^{*(2)}$ and $C_\epsilon^{*(2')}$*

Here we derive the result that underlies Eq. (17):

$$\left\langle \int \boldsymbol{\mu}_2 \cdot \boldsymbol{\mu}_3 f_{12} f_{13} d\mathbf{r}_{12} d\mathbf{r}_{13} \right\rangle_{\omega_1,\omega_2,\omega_3}$$
$$= \left\langle \int \boldsymbol{\mu}_2 \cdot \boldsymbol{\mu}_3 \left(f_{12} + e_{12}^0 \beta u_{12}^{\mathrm{DD}}\right) \left(f_{13} + e_{13}^0 \beta u_{13}^{\mathrm{DD}}\right) d\mathbf{r}_{12} d\mathbf{r}_{13} \right\rangle_{\omega_1,\omega_2,\omega_3} \tag{20}$$

We show in particular that this result does not rely on the orientation average, but applies for any given orientation of the dipoles, $\omega_1, \omega_2, \omega_3$:

$$\int \boldsymbol{\mu}_2 \cdot \boldsymbol{\mu}_3 f_{12} f_{13} d\mathbf{r}_{12} d\mathbf{r}_{13}$$
$$= \int \boldsymbol{\mu}_2 \cdot \boldsymbol{\mu}_3 \left(f_{12} + e_{12}^0 \beta u_{12}^{\mathrm{DD}}\right) \left(f_{13} + e_{13}^0 \beta u_{13}^{\mathrm{DD}}\right) d\mathbf{r}_{12} d\mathbf{r}_{13} \tag{21}$$

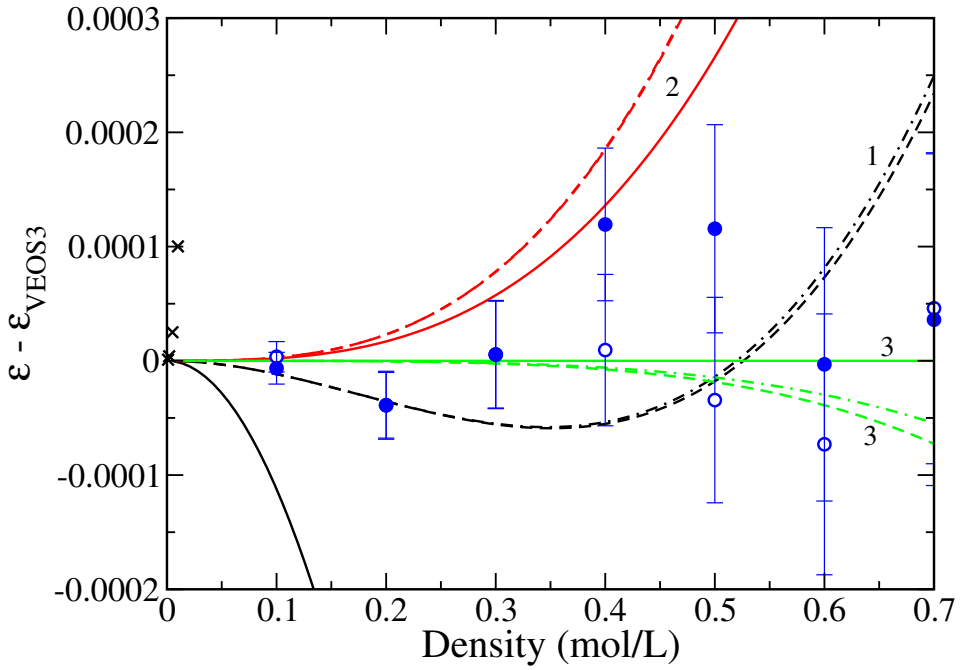

Figure 9. Dielectric constant ϵ of TIP4P water at 500 K, presented as the difference with respect VEOS3 for Eq. (10). Lines and symbols are as in Fig. 8, and numerals next to each line indicate the order of the series used for the calculation, which are also colored as: VEOS1, black; VEOS2, red; VEOS3, green.

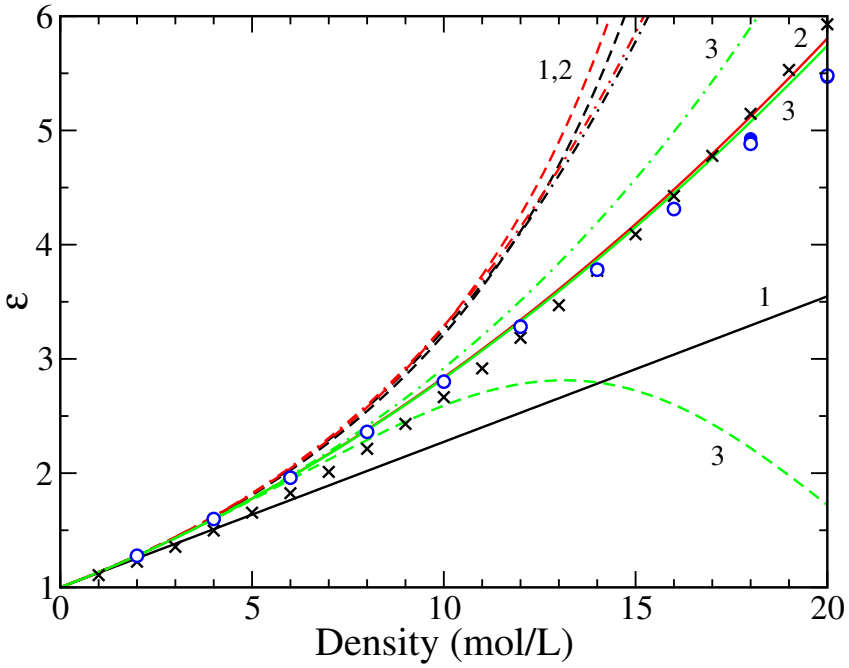

Figure 10. Dielectric constant ϵ of TIP4P water at 680 K ($\beta^*\mu^{*2} = 1.61$). Lines and symbols are as in Fig. 8.

Upon multiplying out the product of the two sums, we see that the modification to the original expression for $C_\epsilon^{*(2)}$ introduces three new terms. Each of these is in fact zero. The development showing this is similar for all three, so we will detail it for only one of them. We have:

$$\int \boldsymbol{\mu}_2 \cdot \boldsymbol{\mu}_3 f_{12} e^0_{13} \beta u^{\mathrm{DD}}_{13} d\mathbf{r}_{12} d\mathbf{r}_{13} \stackrel{?}{=} 0. \tag{22}$$

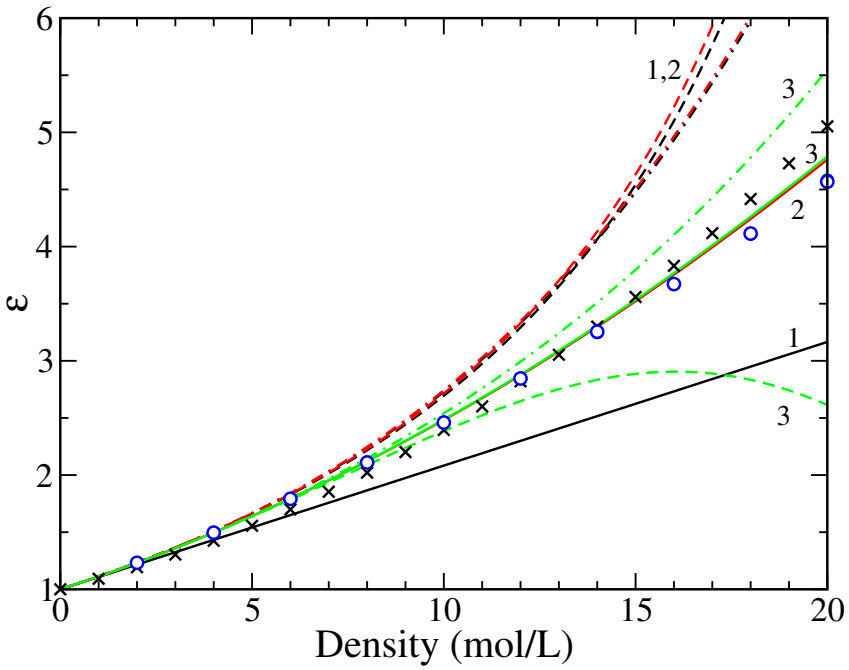

Figure 11. Same as Fig. 10 except data are for temperature of 800 K ($\beta^*\mu^{*2} = 1.37$).

Let us write the integrals more explicitly:

$$\beta^*\mu^{*2}\boldsymbol{\mu}_2\cdot\boldsymbol{\mu}_3\int d\mathbf{r}_{12}f_{12}\int dr_{13}e^0_{13}\left(\frac{\sigma}{r_{13}}\right)^3\int d\hat{\mathbf{r}}_{13}\,(\hat{\boldsymbol{\mu}}_1\cdot\hat{\boldsymbol{\mu}}_3-3(\hat{\boldsymbol{\mu}}_1\cdot\hat{\mathbf{r}}_{13})(\hat{\boldsymbol{\mu}}_3\cdot\hat{\mathbf{r}}_{13}))\stackrel{?}{=}0, \tag{23}$$

which requires that e^0_{13} is spherically symmetric with center at the same position as $u^{\rm DD}_{13}$. The innermost integration, which takes $\hat{\mathbf{r}}_{13}$ over the surface of a unit sphere, is itself zero. This outcome can be obtained via the identity [15]:

$$\int(\mathbf{h}\cdot\hat{\mathbf{s}})\,(\mathbf{k}\cdot\hat{\mathbf{s}})\,d\hat{\mathbf{s}}=\frac{4\pi}{3}\,(\mathbf{h}\cdot\mathbf{k})\,. \tag{24}$$

5.2. *Reaction-field contribution to dielectric virial coefficients*

Here we derive the contribution to the dielectric virial coefficients from the reaction field. The expression for the second dielectric virial coefficient, Eq. (4), can be written for the system with the reaction-field additive pair potential, Eq. (7), as follows:

$$\begin{aligned}B^*_{\epsilon,{\rm RF}(\epsilon')}&=\frac{4\pi}{9}\beta^*\mu^{*2}\left\langle\int(\hat{\boldsymbol{\mu}}_1\cdot\hat{\boldsymbol{\mu}}_2)\,e_{12}e^{\rm RF}_{12}\,d\mathbf{r}^*_{12}\right\rangle_{\omega_1\omega_2}\\&=B^*_\epsilon+\frac{4\pi}{9}\beta^*\mu^{*2}\left[\left\langle\int_0^{r_c^*}(\hat{\boldsymbol{\mu}}_1\cdot\hat{\boldsymbol{\mu}}_2)\,f^{\rm RF}_{12}4\pi r^{*2}_{12}dr^*_{12}\right\rangle_{\omega_1\omega_2}+\left\langle\int_0^{r_c^*}(\hat{\boldsymbol{\mu}}_1\cdot\hat{\boldsymbol{\mu}}_2)\,f_{12}f^{\rm RF}_{12}4\pi r^{*2}_{12}dr^*_{12}\right\rangle_{\omega_1\omega_2}\right]\end{aligned} \tag{25}$$

where $e^{\rm RF}_{12}=\exp(-\beta u^{\rm RF}_{12})$ and $f^{\rm RF}_{12}=e^{\rm RF}_{12}-1$. We are interested large r_c, so we can expand the reaction-field term, using Eq. (7a):

$$f^{\rm RF}_{12}=\mathcal{R}_{\epsilon'}\beta^*\mu^{*2}\,(\hat{\boldsymbol{\mu}}_1\cdot\hat{\boldsymbol{\mu}}_2)\,r_c^{*-3}+O(r_c^{*-6}). \tag{26}$$

When substituted in (25) and the $r_c \to \infty$ limit is taken, the first integral on the right-hand side remains finite, while the second integral is zero for any realistic potential u_{12}. Then

$$\begin{aligned} B^*_{\epsilon,\mathrm{RF}(\epsilon')} &= B^*_\epsilon + \frac{16\pi^2}{27}\left(\beta^*\mu^{*2}\right)^2 \mathcal{R}_{\epsilon'} \left\langle (\hat{\boldsymbol{\mu}}_1 \cdot \hat{\boldsymbol{\mu}}_2)^2 \right\rangle_{\omega_1\omega_2} \\ &= B^*_\epsilon + \frac{16\pi^2}{81}\left(\beta^*\mu^{*2}\right)^2 \mathcal{R}_{\epsilon'} \\ &= B^*_\epsilon + A^{*2}_\epsilon \mathcal{R}_{\epsilon'} \end{aligned} \tag{27}$$

There are two cases of interest. For the self-consistent boundary:

$$\epsilon' = \epsilon(\rho) = 1 + 3A^*_\epsilon \rho + O(\rho^2),$$

which uses Eq. (10), then

$$\mathcal{R}_{\epsilon'} = 2A^*_\epsilon \rho + O(\rho^2).$$

The density-dependent $\mathcal{R}_{\epsilon'}$ means that the reaction-field contribution is made not to B^*_ϵ, but instead to the third-order coefficient C^*_ϵ. To summarize [8]:

$$B^*_{\epsilon,\mathrm{RF}(\epsilon)} = B^*_\epsilon \tag{28a}$$

$$C^*_{\epsilon,\mathrm{RF}(\epsilon)} = C^*_\epsilon + 2A^{*3}_\epsilon \tag{28b}$$

These are the coefficients appearing in Eq. (9). Alternatively, for tin-foil boundary conditions, $\epsilon' = \infty$ and $\mathcal{R}_{\epsilon'} = 1$, and we have

$$B^*_{\epsilon,\mathrm{RF}(\infty)} = B^*_\epsilon + A^{*2}_\epsilon, \tag{29a}$$

consistent with Eq. (10). We have not similarly derived $C^*_{\epsilon,\mathrm{RF}(\infty)}$ by introducing e^{RF}_{ij} in Eq. (5); instead we deduce from Eq. (8) and Eq. (10) (the latter may be derived from Eqs. (2) or (9)) that it should be

$$C^*_{\epsilon,\mathrm{RF}(\infty)} = C^*_\epsilon + 2A^*_\epsilon B^*_\epsilon + A^{*3}_\epsilon. \tag{29b}$$

References

[1] M.P. Allen and D.J. Tildesley, *Computer simulation of liquids* Oxford science publications (, , 1987).
[2] M. Neumann, Mol. Phys. **50** (4), 841 (1983).
[3] A.J. Schultz, S.G. Moustafa, W. Lin, S.J. Weinstein and D.A. Kofke, J. Chem. Theory Comput. **12** (4), 1491 (2016).
[4] D.W. Jepsen, J. Chem. Phys. **44** (2), 774 (1966).
[5] C. Joslin, Mol. Phys. **42** (6), 1507 (1981).
[6] C.G. Gray, K.E. Gubbins and C.G. Joslin, *Theory of Molecular Fluids*, Vol. 2: Applications (, , 2011).
[7] J.G. Kirkwood, J. Chem. Phys. **7** (10), 911 (1939).
[8] C. Joslin and S. Goldman, Mol. Phys. **79** (3), 499 (1993).
[9] A.D. Buckingham and J.A. Pople, Trans. Faraday Soc. **51**, 1029 (1955).
[10] A. Buckingham and C. Joslin, Mol. Phys. **40** (6), 1513 (1980).
[11] J. Powles and E. McGrath, Mol. Phys. **43** (3), 641 (1981).
[12] A.J. Stone, Y. Tantirungrotechai and A.D. Buckingham, Phys. Chem. Chem. Phys. **2** (4), 429 (2000).
[13] J. Dymond and E. Smith, Trans. Faraday Soc. **60**, 1378 (1964).
[14] G.S. Rushbrooke, Mol. Phys. **37** (3), 761 (1979).
[15] G. Rushbrooke and R. Shrubsall, Mol. Phys. **55** (3), 599 (1985).
[16] H. Sutter and R.H. Cole, J. Chem. Phys. **52** (1), 132 (1970).
[17] W.L. Jorgensen and J.D. Madura, Mol. Phys. **56** (6), 1381 (1985).
[18] W. Stockmayer, J. Chem. Phys. **9** (12), 863 (1941).
[19] W.L. Jorgensen, J. Chandrasekhar, J.D. Madura, R.W. Impey and M.L. Klein, J. Chem. Phys. **79** (2), 926 (1983).
[20] E.A. Elfimova, A.O. Ivanov, J.O. Sindt and P.J. Camp, Mol. Phys. **113** (23), 3717 (2015).
[21] A.D. Buckingham and J.A. Pople, Trans. Faraday Soc. **51**, 1179 (1955).
[22] J. Kolafa and L. Viererblova, J. Chem. Theory Comput. **10** (4), 1468 (2014).
[23] C. Zhang and M. Sprik, Physical Review B **93**, 144201 (2016).
[24] J.K. Singh and D.A. Kofke, Phys. Rev. Lett. **92** (22), 220601 (2004).
[25] K.M. Benjamin, A.J. Schultz and D.A. Kofke, J. Phys. Chem. B **113**, 7810 (2009).
[26] K.M. Benjamin, A.J. Schultz and D.A. Kofke, J. Phys. Chem. C **111**, 16021 (2007).

[27] K.M. Benjamin, J.K. Singh, A.J. Schultz and D.A. Kofke, J. Phys. Chem. B **111**, 11463 (2007).
[28] K.M. Benjamin, A.J. Schultz and D.A. Kofke, Ind. Eng. Chem. Res. **45**, 5566 (2006).
[29] C. Kriebel and J. Winkelmann, Mol. Phys. **90** (2), 297 (1997).
[30] D.P. Fernandez, A. Goodwin, E.W. Lemmon, J. Sengers and R.C. Williams, J. Phys. Chem. Ref. Data **26** (4), 1125 (1997).
[31] M. Lísal, W.R. Smith and I. Nezbeda, Fluid Phase Equilib. **181**, 127 (2001).
[32] W. Wagner and A. Prußb, J. Phys. Chem. Ref. Data **31** (2), 387 (2002).